Nanoscale

PAPER

View Article Online
View Journal | View Issue

Check for updates

Cite this: *Nanoscale*, 2023, **15**, 14800

Magnetic PiezoBOTs: a microrobotic approach for targeted amyloid protein dissociation†

Shen Ning,‡[a] Roger Sanchis-Gual,‡[b] Carlos Franco,*[b] Pedro D. Wendel-Garcia,[c] Hao Ye,[b] Andrea Veciana,[b] Qiao Tang,[b] Semih Sevim,[b] Lukas Hertle,[b] Joaquin Llacer-Wintle,[b] Xiao-Hua Qin,[d] Caihong Zhu,[e] Jun Cai,[f] Xiangzhong Chen,[b] Bradley J. Nelson,[b] Josep Puigmartí-Luis*[g,h] and Salvador Pané *[b]

Piezoelectric nanomaterials have become increasingly popular in the field of biomedical applications due to their high biocompatibility and ultrasound-mediated piezocatalytic properties. In addition, the ability of these nanomaterials to disaggregate amyloid proteins, which are responsible for a range of diseases resulting from the accumulation of these proteins in body tissues and organs, has recently gained considerable attention. However, the use of nanoparticles in biomedicine poses significant challenges, including targeting and uncontrolled aggregation. To address these limitations, our study proposes to load these functional nanomaterials on a multifunctional mobile microrobot (PiezoBOT). This microrobot is designed by coating magnetic and piezoelectric barium titanate nanoparticles on helical biotemplates, allowing for the combination of magnetic navigation and ultrasound-mediated piezoelectric effects to target amyloid disaggregation. Our findings demonstrate that acoustically actuated PiezoBOTs can effectively reduce the size of aggregated amyloid proteins by over 80% in less than 10 minutes by shortening and dissociating constituent amyloid fibrils. Moreover, the PiezoBOTs can be easily magnetically manipulated to actuate the piezocatalytic nanoparticles to specific amyloidosis-affected tissues or organs, minimizing side effects. These biocompatible PiezoBOTs offer a promising non-invasive therapeutic approach for amyloidosis diseases by targeting and breaking down protein aggregates at specific organ or tissue sites.

Received 25th May 2023,
Accepted 17th August 2023

DOI: 10.1039/d3nr02418k

rsc.li/nanoscale

Open Access Article. Published on 18 avgust 2023. Downloaded on 8. 01. 2026 04:58:24.
This article is licensed under a Creative Commons Attribution-NonCommercial 3.0 Unported Licence.

Introduction

Amyloidosis is a group of diseases in which abnormal extracellular protein misfolding results in insoluble and aggregated β-sheet fibrillar protein that accumulates in body tissues and organs.[1] Typically, amyloidosis diseases are caused by a variety of proteins, including transthyretin,[2] antibody light chains,[3] and β2-microglobulin,[4] whose accumulation can be localized to a single organ or be systemic. Standard treatments for amyloidosis, such as chemotherapy, steroids, and targeted therapies, focus on preventing further amyloid aggregation and accumulation.[5,6] However, the early mortality rate, between 25% to 30%, has remained constant in the last decades, due in part to the lack of tools for early diagnosis as well as the limited treatment options once the disease clinically manifests.[3] Therefore, experimental treatments, including monoclonal antibodies,[7] small molecules,[8] and gene therapies,[8] have also been explored. Despite these efforts, effective therapies for amyloidosis remain challenging, and more research is needed to develop treatments that can halt or reverse the disease's progression.

To address this medical challenge, piezoelectric materials, can introduce a new therapeutic modality by means of piezoelectric effect. Under mechanical stimulation, piezoelectric materials can deform their crystalline structure, generating a piezoelectric potential that induces an electric field.[9–11] In

[a]*Boston University School of Medicine, Boston, MA, USA*
[b]*Multi-Scale Robotics Lab, Institute of Robotics and Intelligent Systems, ETH Zürich, Tannestrasse 3, CH-8092 Zürich, Switzerland. E-mail: carlos.franco@chem.ethz.ch, vidalp@ethz.ch*
[c]*Institute of Intensive Care Medicine, University Hospital Zurich, Zurich, Switzerland*
[d]*Institute for Biomechanics, ETH Zürich, Leopold-Ruzicka-Weg 4, CH-8093 Zürich, Switzerland*
[e]*School of Basic Medical Sciences, State Key Laboratory of Medical Neurobiology, Fudan University, Shanghai, China*
[f]*School of Mechanical Engineering and Automation, Beihang University, No. 37 Xueyuan Road, Haidian District, Beijing, 100191, China*
[g]*Departament de Ciència dels Materials i Química Física, Institut de Química Teòrica i Computacional, University of Barcelona (UB), 08028 Barcelona, Spain. E-mail: josep.puigmarti@ub.edu*
[h]*ICREA, Institució Catalana de Reserca i Estudis Avançats, Pg. Lluís Companys 23, 08010 Barcelona, Spain*

†Electronic supplementary information (ESI) available. See DOI: https://doi.org/10.1039/d3nr02418k

‡These authors contributed equally to this work.

This journal is © The Royal Society of Chemistry 2023

Open Access Article. Published on 18 avgust 2023. Downloaded on 8. 01. 2026 04:58:24.
This article is licensed under a Creative Commons Attribution-NonCommercial 3.0 Unported Licence.

addition, the fundamental properties of piezoelectric materials allow for their actuation in a wireless and safe manner *via* mechanical vibrations such as ultrasound.[12] On this basis, piezoelectric nanomaterials have been used to develop alternative therapies with remarkable efficacy. For example, under mechanical stimulation, piezoelectric nanoparticles (NPs) can promote the proliferation and differentiation of adult stem cells into neurons,[13–15] as well as tissue regeneration by piezoelectric cell stimulation.[16,17] Additionally, the piezoelectric effect can catalyse electrochemical reactions, enabling for example the production of reactive oxygen species (ROS) in water,[12] which have demonstrated high efficiency for cancer treatments.[18,19] Recently, Park *et al.* have shown that the ROS produced by biocompatible piezoelectric NPs under mechanical actuation can also be used to effectively dissociate protein aggregates such as Alzheimer's β-amyloid.[20,21] These findings offer promising applications for amyloidosis therapy. Nevertheless, the utilization of these piezoelectric NPs faces some challenges for their practical biomedical application due to (i) their targeting, which requires their functionalization and thus, the use of appropriate biocompatible ligands (or other molecules) that can interact specifically with target cells or tissues;[22] (ii) their aggregation, which can result in their off-targeted accumulation in various organs and tissues, potentially inducing side effects;[23] and (iii) difficulties in localizing them due to their small size and complex interactions with biological systems.[24]

Thus, in this work, to achieve the full potential of piezoelectric NPs for amyloidosis therapy, we propose integrating them onto magnetically navigated microrobots (PiezoBOTs, Fig. 1A). Microrobots can perform minimally invasive procedures by accessing difficult-to-reach regions of the human body thanks to both their small dimensions and untethered motion capabilities.[25,26] To this end, barium titanate ($BaTiO_3$ (BTO)) NPs are employed due to their excellent biocompatibility[27] and high piezoelectric coefficient and dielectric constant, which results in a high piezocatalytic effect.[28,29] To integrate the BTO NPs on the magnetic microrobots, we adopt a biotemplating approach exploiting the helical structure of the cyanobacterium *Spirulina platensis* as a microrobotic scaffold.[30–33] Accordingly, our PiezoBOTs, which combine magnetic navigation and ultrasound-mediated piezoelectric effect, show excellent targeting of amyloid disaggregation with minimum side effects in less than 10 min (Fig. 1B and C). Taken together, these characteristics make the PiezoBOTs a flexible tool for minimally invasive amyloidosis therapy.

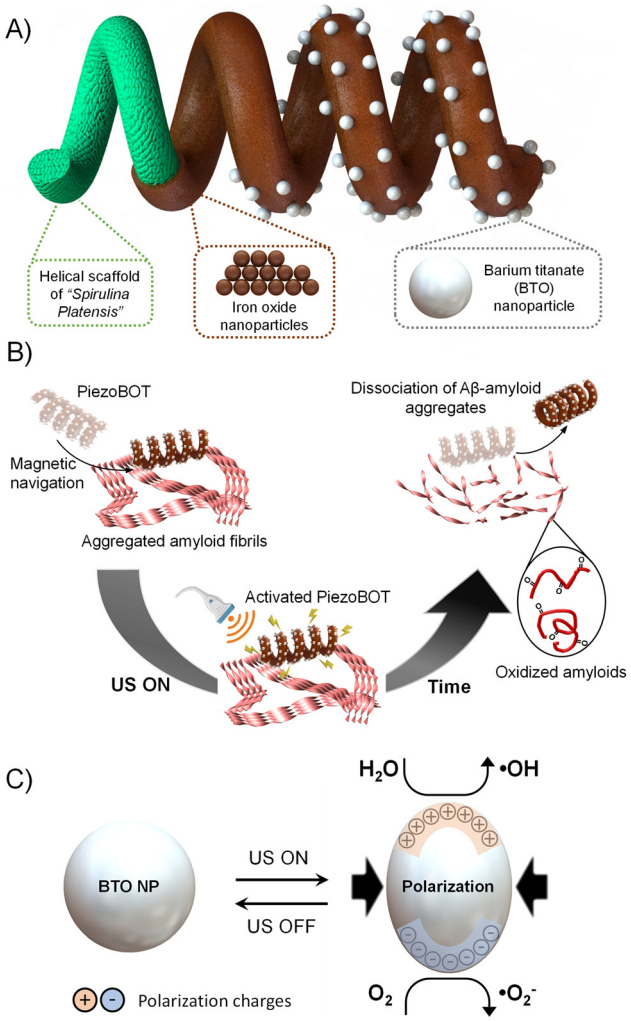

Fig. 1 (A) Scheme of the structure of the PiezoBOT. *Spirulina platensis* biotemplates are covered by a layer of magnetic nanoparticles and another layer of piezoelectric nanoparticles. (B) Magnetic navigation and PiezoBOT actuation to dissociate amyloid aggregates. The Aβ fibril structures are dissociated due to the oxidation of the amino acid residues and the disruption of the hydrophobic interactions and hydrogen bonds. (C) ROS generation through the piezoelectric effect.

Experimental

Synthesis of $BaTiO_3$ nanoparticles

BTO nanoparticles were synthesized by mixing 56 g of NaOH and 3.195 g of TiO_2 in 140 mL of DI water. Then, the solution was stirred and sonicated and kept covered with parafilm. The solution is then heated in an autoclave at 240 °C for 24 h. The product, $H_2Ti_3O_7$, was washed with 0.2 mol L^{-1} HCl solution, DI water and ethanol before drying at 80 °C overnight. 2.208 g of $Ba(OH)_2{\cdot}8H_2O$ and 0.2576 g of $H_2Ti_3O_7$ were added in 35 mL of DI water and heated at 240 °C for 12 hours in an autoclave. The final product, $BaTiO_3$, was washed with 0.2 mol L^{-1} HCl solution, DI water and ethanol before drying at 80 °C overnight. The non-piezoelectric BTO nanoparticles with cubic phase (purchased from Sigma) were used as an additional control.

Magnetic *Spirulina platensis* biotemplates

Magnetic templates were prepared following the fabrication process reported by Terzopoulou *et al.*[30] Firstly, iron oxide nanoparticles were synthesized with a co-precipitation method: an aqueous solution of $FeCl_3$ (8 mM) and $FeCl_2$ (16 mM) was heated at 50 °C and 0.5 M NaOH solution was

Open Access Article. Published on 18 avgust 2023. Downloaded on 8. 01. 2026 04:58:24.
This article is licensed under a Creative Commons Attribution-NonCommercial 3.0 Unported Licence.

dropwise added. A black suspension was formed, and the mixture was sonicated for 60 minutes. The particles were then collected and 100 μL of 5 M HCl was added to bring the pH to the acidic range. In parallel, *Spirulina platensis* was implemented as biotemplate for the magnetic template fabrication. The magnetic coating was performed by incubating the templates with the Fe_3O_4 nanoparticles for 72 h under stirring. The coated biotemplates were collected after multiple wash steps. In the final wash step, the solution was instantly frozen in liquid nitrogen and freeze-dried overnight. The dried magnetic templates were stored in ambient conditions for future use. For attaching BTO NPs, gelatin–glycerol coating of the magnetic templates was performed as follows: 30 mg of gelatin was dissolved in 1 mL of water at 55 °C under continuous shaking at 800 rpm. 30 mL of glycerol was added along with 2 mg of magnetic templates. The mixture was homogenized for 10 minutes. Two washing steps (first with hot and then with cold water) were performed, before BTO particles (with a concentration of 2 mg mL^{-1}) were introduced. The coating time of the magnetic templates with the BTO was 2 hours. Multiple wash steps with water were then performed, and the final PiezoBOTs were collected *via* magnetic separation.

Microfluidic device fabrication for magnetic navigation

The master mold of microfluidic devices was fabricated on a silicon wafer (Okmetic, Finland) coated with SU-8 2150 photoresist (Microchem, USA) using standard photolithography techniques. Subsequently, conventional soft lithography methods (*i.e.* poly-dimethylsiloxane (PDMS) replica molding) were used to replicate the 200 μm-high microchannel structures patterned on the master mold.[34] First, the silicon master mold was passivated with chlorotrimethylsilane (Sigma-Aldrich Chemie GmbH, Switzerland) under vacuum for 30 minutes. Then a 10 : 1 (in weight) mixture of PDMS elastomer and curing agent (Sylgard 184, Dow Corning, USA) was prepared and placed under vacuum for 30 minutes to remove trapped gas. The degassed PDMS mixture was poured on top of the master mold and cured in an oven (at 80 °C) for overnight. After the curing process, the PDMS slab was removed from the master mold and cut using a razor blade. Inlets and outlets holes of the microfluidic device were then punched using a 1.5 mm biopsy puncher (Miltex GmbH, Germany). Finally, the PDMS microfluidic device was bonded to a glass substrate (24 mm × 60 mm, Menzel Glasbearbeitungswerk GmbH & Co. KG, Germany) using oxygen plasma activation.

Microrobot locomotion

The experiments were conducted using a commercially available magnetic actuation system MFG-100 manufactured by MagnebotiX AG (Switzerland). Simultaneously, bright field images were recorded using an inverted microscope.

SH-SY5Y cell culture and toxicity assays

SH-SY5Y cells were cultured in 40% of DMEM + GlutaMAX (with 1× Antibiotic–Antimycotic) and 40% MEM + GlutaMAX with 1% FBS. Cells were plated in 96 wells at 10 000 cells per well. The cells were allowed to grow overnight for 24 hours at 37 °C and 5% CO_2. PiezoBOTs were added to the media and incubated for 24 hours at 37 °C. For the MTT assay (Invitrogen M6494), 0.5 mg mL^{-1} of the substrate was added in each 96 well. The cells were incubated for 4 hours at 37 °C and 5% CO_2, and after the incubation, the medium was removed, and 50 μL (96 well plate) or 1 mL (24 well plate) of dimethyl sulfoxide was added to dissolve the water-insoluble generated formazan crystals. Samples of each well were taken and the absorbance at 570 nm was measured in a microplate reader (Infinite M200 Pro, Tecan AG) taking a reference measurement at 630 nm to normalize the data. In the case of samples containing microrobots, the absorbance of a blank (where the same amount of MTT was incubated in presence of the microrobots without any cells) was subtracted.

Temperature experiments

A Fluke thermal imaging camera was used to record the temperature changes in a 200 μL PBS solution at various ultrasound power levels. Fluke software was used to extract the obtained results.

Aβ42 aggregation

Aβ(1–42) peptides, or Aβ42, were diluted with a proprietary buffer solution (solution A) to a final concentration of 2.5 mg ml^{-1} and sonicated for 3–5 minutes. Then, the previous solution was diluted to 0.2 mg mL^{-1} and 100 μL were incubated at 37 °C and 1200 rpm overnight.

Aβ42 aggregation kinetics

10 μL of 2 mM ThioT was added to 90 μL of the diluted Aβ42 peptide. The solution was placed in a fluorescence plate reader at 37 °C with 15 seconds shaking and read every 10 minutes at Ex/Em = 440 nm/484 nm for 4 hours.

Microrobot incubation and Aβ42 disaggregation (hand-held ultrasound)

For microrobot-assisted Aβ disaggregation, microrobots (0.12 mg mL^{-1}) were incubated with pre-aggregated Aβ42 (0.12 mg mL^{-1}) in a 96-well plate. A hand-held ultrasound (Roscoe Medical, US Pro 2000 2nd edition, 1 MHz, low power = 0.32 W ± 20%, medium power = 3.2 W ± 20%, high power = 6.4 W ± 20%) was then applied to the bottom of the plate for 1 min × 10 cycles. 2 minutes of rest period was applied between cycles.

BTO incubation and Aβ42 disaggregation (bath sonicator)

100 μL of 6 mg mL^{-1} of BTO was incubated with 100 μL of 0.24 mg mL^{-1} of pre-aggregated Aβ42. Ultrasound stimulation (Bandelin Sonocool 255) was applied for 1–2 hours at 75% power, in a controlled ultrasound bath (VWR BA-3500, nominal power and frequency: 150 W, 35 kHz) at 24 °C.

Physical characterization

Zetasizer was used to perform DLS measurements. The crystalline phase was measured by X-ray diffraction (Bruker AXS D8

 This journal is © The Royal Society of Chemistry 2023

Open Access Article. Published on 18 avgust 2023. Downloaded on 8. 01. 2026 04:58:24.
This article is licensed under a Creative Commons Attribution-NonCommercial 3.0 Unported Licence.

Advance, Cu Kα, (Billerica, MA). IR spectra were measured on an ATI Mattson Genesis Series FTIR instrument over the range of 500–4000 cm^{-1}. Optical images were taken using an Olympus IX81 microscope. For BTO TEM measurements, samples immersed in water were dropped on grids (carbon film coated copper, 400 mesh; Ted Pella, Inc. 01824) and allowed to dry in air overnight. TEM images were captured on FEI Talos F200X (Chem S/TEM) operating at 150 kV. Amyloid peptide TEM samples were prepared on glow discharged (PELCO easiGlow, Ted Pella, USA) carbon-coated grids (Quantifoil, D) for 120 s. The excess of fluid was removed with filter paper and the grids were washed two times with distilled water. The wet samples were stained with a drop of 2% uranyl acetate for 1 s, followed by a second step of 15 s. Excess moisture was drained with filter paper, and the imaging of the air-dried grids was done with a TEM Morgagni 268 (Thermo Fisher Scientific, USA) operated at 100 kV. SEM images were obtained with Zeiss ULTRA 55 plus equipment at 20 kV. A drop of the sample dispersion was cast on a Si substrate that had previously been cleaned in acetone, isopropanol, and DI water. Samples with pure spirulina were sputtered with a thin layer of Au prior to imaging.

Results and discussion

Fabrication of spirulina biotemplated PiezoBOTs

To fabricate our spirulina biotemplated PiezoBOTs, we followed the step-wise scheme depicted in Fig. 2A. At first, we coated 70 ± 30 μm long helical microstructures based on the biotemplate spirulina with pre-synthesized magnetic iron oxide NPs of *ca.* 10–20 nm. We specifically selected Fe_3O_4 NPs due to their high biocompatibility and low cytotoxicity.[34,35] In this process, the negatively charged surface of the spirulina electrostatically interacts with the positively charged Fe_3O_4 NPs, allowing their fixation onto the surface. Then, we functionalized the surface of the microhelical template with glycerin-plasticized glycerol, which can act as an adhesion layer enabling the fixation of further functional materials by means of the amino and carboxylic functional groups.[32] Accordingly, we used this concept to decorate our microhelices with an additional layer of pre-synthesized barium titanate (BTO) piezoelectric NPs, thus obtaining our PiezoBOTs. Note that the employed BTO NPs were pre-synthesized using a hydrothermal methodology (further details can be found in the Methods section). These NPs exhibit a spherical-like morphology (Fig. 2C and S1A†) with a size distribution centered at *ca.* 300 nm (Fig. S1B†). Importantly, their powder X-ray diffraction (XRD) pattern (Fig. S1C†) shows a peak splitting at 45°, indicating that the XRD pattern of BTO corresponds to the tetragonal phase, confirming the piezoelectric nature of the NPs.[9] Further XRD analysis was conducted to characterize the crystalline structure of the magnetic and piezoelectric NPs once attached to the helical scaffold. The obtained crystalline patterns of BTO NPs, magnetic spirulina (spirulina@Fe_3O_4) and PiezoBOT (spirulina@Fe_3O_4@BTO) are compared in Fig. 2D. The presence of Fe_3O_4 and BTO peaks in the PiezoBOT evidence that their crystalline structure is preserved after their incorporation and the nanoparticles were successfully decorated on the spirulina microstructure.

The adequate integration of the functional materials that compose our PiezoBOTs into the biotemplated chassis was

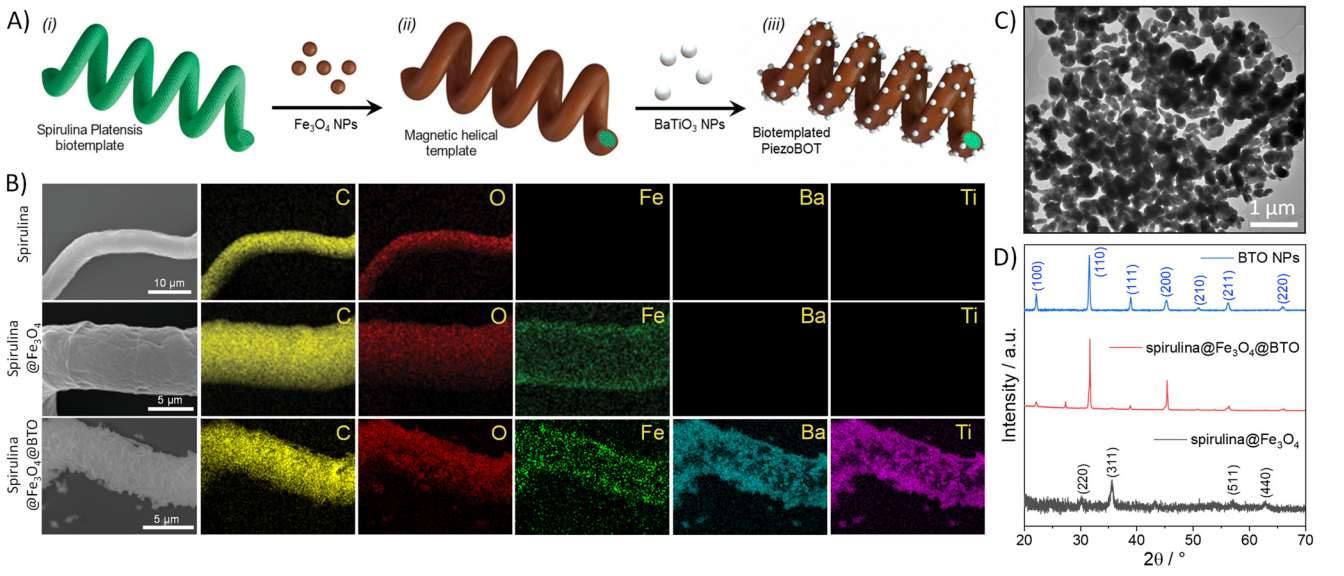

Fig. 2 (A) Fabrication steps of magnetic PiezoBOTs: (i) preparation of the *Spirulina platensis* biotemplate, (ii) fixation of iron oxide NPs on the biotemplate, and (iii) surface functionalization and attachment of BTO NPs to the biotemplate. (B) SEM images and EDX mapping of spirulina, spirulina@Fe_3O_4 and spirulina@Fe_3O_4@BTO. (C) TEM image of BTO NPs. (D) PXRD patterns of BTO nanoparticles, spirulina coated with iron oxide nanoparticles, and PiezoBOTs (spirulina coated with iron oxide and BTO nanoparticles). Iron oxide peaks correspond to cubic inverse spinel structure[43] and BTO peaks to BTO tetragonal phase.[44]

Open Access Article. Published on 18 avgust 2023. Downloaded on 8. 01. 2026 04:58:24.
This article is licensed under a Creative Commons Attribution-NonCommercial 3.0 Unported Licence.

analyzed by scanning electron microscopy (SEM). Noticeable morphology differences can be observed between the microrobot surface during the different fabrication steps (Fig. 2B). While the unmodified spirulina has a smooth surface, the surface morphology exhibits a particulated texture after modification with the magnetic Fe_3O_4 NPs. Notably, after attaching the BTO NPs onto the microhelix, the roughness of the microrobots increases. In addition to the SEM morphology characterization, we investigated the elemental composition of the PiezoBOTs by means of energy-dispersive X-ray spectroscopy (EDX) (Fig. 2B). Besides the carbon and oxygen from the biotemplate, spirulina@Fe_3O_4 presents a uniform iron signal all over the spiral structure due to the Fe_3O_4 magnetic NPs. Furthermore, after introducing BTO NPs, the PiezoBOTs display a representative barium and titanium EDX signal. Note that the barium and titanium distributions are uniform in the microhelices confirming the homogenous allocation of the BTO along the entire microrobot's surface.

Microrobot magnetic navigation

Thanks to the homogeneous distribution of the magnetic NPs along the surface, our PiezoBOTs can be easily manipulated by a 5 degree-of-freedom setup equipped with 8 electromagnets. Video S1† shows a microrobot able to swim by corkscrewing using low rotating magnetic fields. Magnetic field gradients can be applied to operate the microrobots in the *z*-axis, thus reducing the micromotor–surface interactions. Note that the velocity and trajectory of magnetic microrobots are strongly dependent on the frequency of the applied magnetic field, as previously reported.[32,36] Adequate speed and controllability are achieved at a rotating field frequency of 1 to 3 Hz. There was no spiral or lateral movement beyond 3 Hz. Concerning the influence of the magnetic field on the microrobot locomotion, an increase in this magnitude results in higher velocities (Fig. S2†). However, while the drift velocity shows a slight increase, the forward velocity is significantly improved. The highest ratio of forward velocity to drift velocity is achieved when applying a magnetic field between 8 and 15 mT. Furthermore, magnetic navigation was achieved in DI water (Fig. 3A, B and Video S2†) as well as in a microfluidic vasculature model in free PBS solution (Fig. 3C–E and Video S3†). The microfluidic model recapitulates the divergence of the vascular path from one vessel to three different paths. To demonstrate the delivery capability of our microrobot to overcome challenging vascular pathways, the microrobot was successfully directed around a sharp corner not typically achievable with traditional catheter navigation, highlighting the ability to control PiezoBOTs through extremely tortuous vasculature (Fig. 3D and E).

PiezoBOT biocompatibility

After evaluating the navigation capabilities of the PiezoBOTs, we analyzed their biocompatibility features. In this regard, we carried out MTT assays to determine cell metabolic activity in SH-SY5Y cells after 24 hours in the presence of PiezoBOT at different concentrations. SH-SY5Y is a neuroblastoma cell line

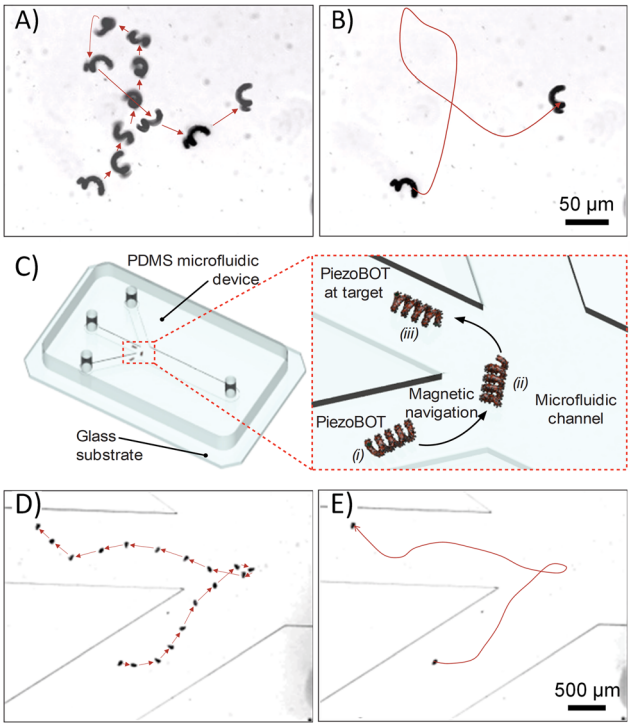

Fig. 3 (A and B) Time-lapse images showing the trajectory of a PiezoBOT under magnetic manipulation in DI water. (C) Scheme of the PDMS microfluidic device. (D and E) Trajectory of a PiezoBOT under magnetic manipulation in PBS solution in a microfluidic vasculature model.

that has been widely used as a model to study the biocompatibility of materials that will come into contact with nerve tissue. When incubated with PiezoBOTs, high viabilities (above the cytotoxicity level (80%; ISO 10993-5:2009)) are found for values below 0.12 mg mL^{-1} (Fig. 4A), demonstrating the excellent biocompatibility of these microstructures. Next, the impact of piezoelectricity on the cell viability at different ultrasound power levels was investigated in the presence of PiezoBOTs (Fig. 4B). In particular, acoustic stimulation at low (0.32 W), medium (3.2 W), and high power (6.4 W) at 1 MHz from a hand-held ultrasound were tested. The obtained values show that, when low or medium ultrasound power is applied, the viability is slightly affected even at longer times (>5 min). In contrast, the biocompatibility sharply decreases up to less than 20% with high ultrasound power. We attributed this cytotoxicity level to the sharp increase in temperature of the cell media, which rises to over 50 °C in less than 2 minutes when high power is applied (Fig. S3†), while for medium and low power, the temperature does not exceed 36 °C after 1.5 minutes. Note that ROS generation induced by BTO actuation can also trigger cell death *via* oxidative stress mechanisms.[37] However, given the intrinsic antioxidant defenses exhibited by neuronal cells[38,39] and the fact that any temperature above 45 °C can cause thermotoxicity to cells,[40] we concluded that temperature changes in our experiments are pri-

This journal is © The Royal Society of Chemistry 2023

Open Access Article. Published on 18 avgust 2023. Downloaded on 8. 01. 2026 04:58:24.
This article is licensed under a Creative Commons Attribution-NonCommercial 3.0 Unported Licence.

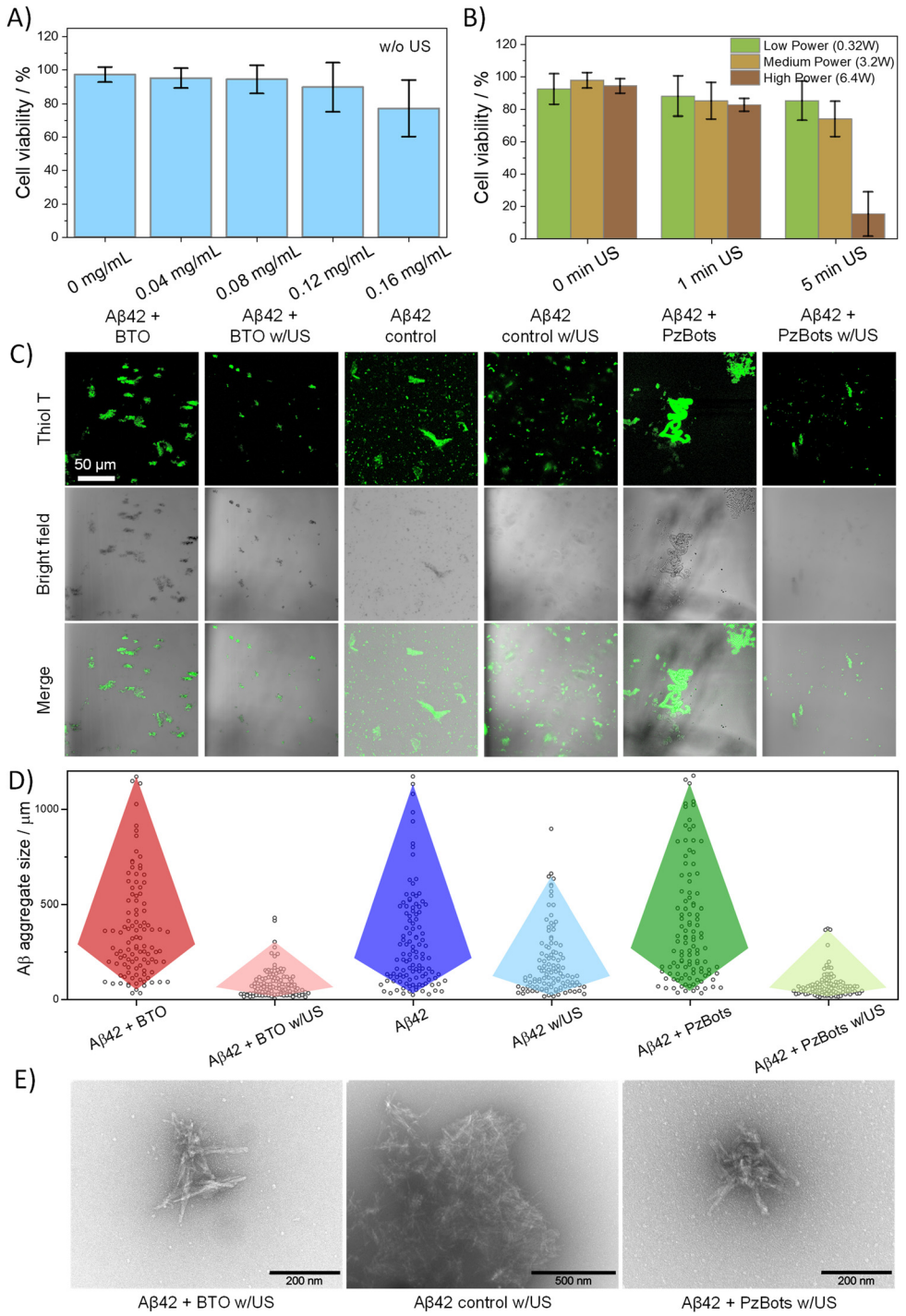

Fig. 4 (A) MTT assays with SH-SY5Y cells. PiezoBOT cytotoxicity at various concentrations after 24 hours of incubation. (B) Cytotoxicity of 0.12 mg mL^{-1} PiezoBOTs after 24 hours of incubation after being subjected to different ultrasound power levels and times. (C) Confocal images before and after ultrasound stimulation. (D) Histograms of the aggregate size of the different samples. (E) TEM images of the different samples after ultrasound stimulation.

marily responsible for cell death. As a result, to maintain a safe temperature while maximizing the piezoelectric performance of our PiezoBOTs, we selected multiple stimulation cycles at low or medium ultrasound power of 1-minute duration interspersed with resting periods.

Amyloid disaggregation *via* ultrasound-activated PiezoBOTs

The performance of our PiezoBOTs to disaggregate tight amyloid protein aggregates was evaluated by employing Aβ42 proteins under acoustic stimulation. Aβ42 proteins were

Open Access Article. Published on 18 avgust 2023. Downloaded on 8. 01. 2026 04:58:24.
This article is licensed under a Creative Commons Attribution-NonCommercial 3.0 Unported Licence.

chosen because they form a major component of amyloid plaques, accumulating in neurons and extracellularly in Alzheimer's disease brains. These proteins are synthetically available, can easily oligomerize into fibril structures similar to those in amyloidosis, and thus provide an ideal model for studying aggregation/disaggregation processes. The proteins were pre-aggregated into fibrillar structures (see Methods section) and validated *via* aggregation kinetics using a Thioflavin T (ThT) assay kit (Fig. S4†).

To study the efficacy of our PiezoBOTs as amyloidosis therapeutics, first we analyzed the piezoelectric performance of the bare BTO NPs on Aβ42 disaggregation. To this end, we pre-aggregated and incubated the proteins with BTO NPs and applied ultrasound stimulation using a controlled handheld ultrasound device to simulate a clinical treatment scenario.

To maximize piezoelectric efficiency and in accordance with the previous cytotoxicity experiment avoiding any thermotoxic effects, 10 cycles of 1 minute ultrasound stimulation and 2 minutes of interspersed resting periods were performed at a medium power level of 3.2 W. The resulting sizes of amyloid aggregates were studied by combining confocal imaging, transmission electron microscopy (TEM) and dynamic light scattering (DLS) measurements.

Initially, we compared the size of amyloid aggregates labelled with ThT using confocal microscopy before and after subjecting them to 10 cycles of ultrasound treatment (see Fig. 4C). We specifically used ThT as a biomarker because it binds to the β-sheet structure present in amyloid aggregates, resulting in an increased fluorescence signal that allows for easy detection. Notably, the presence of BTO NPs did not significantly impact the size of the amyloid aggregates. However, following ultrasound treatment, the size of Aβ42 aggregates was reduced by 80% (Fig. 4D). In contrast, in the absence of BTO NPs, the size distribution of Aβ42 aggregates was reduced by only 43% following ultrasound stimulation. Similar trends were also observed by DLS measurements (ESI Fig. S5†), showing that the particle size distribution of the Aβ42 proteins decreases after the piezoelectric treatment with the BTO NPs. To gain more insight into the amyloid dissociation, we examined the effect of BTO and ultrasound on the morphology of the Aβ42 aggregates by scanning and transmission electron microscopy (SEM and TEM). As shown in Fig. S6,† the pre-aggregated Aβ42 amyloids are formed by the assembly of elongated fibrils, whereas the non-aggregated amyloids consist of individual long fibers. By ultrasound stimulation (Fig. 4E), the fibrils are cut into shorter ones producing a significant reduction in the aggregate size. In contrast, in the presence of BTO NPs, the Aβ42 fibrillar aggregates are broken down into smaller sizes and the resulting aggregates are composed of a lower number of fibrils.

Overall, these observations suggest that the piezoelectric effect induced by BTO NPs contributes significantly more to protein disaggregation than the mechanical effect of ultrasound. To clearly verify the piezocatalytic performance of BTO NPs for Aβ42 fibrils dissociation, we compared it with non-piezoelectric cubic BTO NPs (cBTO). Specifically, we selected the cubic phase of BTO NPs because they can be obtained in a similar size to the tetragonal BTO but without displaying piezoelectricity (further physical detail of cBTO can be found in ESI Fig. S1†). As shown in the confocal images in Fig. S7,† after actuating the cBTO NPs, the resulting aggregates show a similar size to the experiments realized after applying ultrasounds without piezoelectric NPs. The latter demonstrates that the piezoelectric effect induced by tetragonal BTO NPs is responsible for the majority of Aβ42 fibrils dissociation, rather than other mechanic phenomena such as cavitation or flexocatalysis.[21]

Subsequently, we investigated the role of the piezocatalytically generated oxidative species in the disaggregation process of Aβ42 fibrils. As previously reported, ROS can destabilize Aβ fibril structures by both oxidizing the amino acid residues and disrupting the hydrophobic interactions and hydrogen bonds.[21,41,42] Therefore, considering the detection of ROS such as $^{\bullet}OH$ during the BTO actuation through scavenger-quenching experiments (Fig. S8†), we confirmed that the dissociation process of Aβ42 fibrils is associated with the generation of these oxidative species.

After studying the piezocatalytic effect on Aβ42 disaggregation, the effectiveness of PiezoBOTs was evaluated and compared. When the amyloids were subjected to ultrasound in the presence of these microstructures, a reduction of the amyloid size by 79% was observed by confocal imaging (Fig. 4C and D). Importantly, this size decrease is comparable to that obtained when using free BTO NPs, confirming the excellent capabilities of the PiezoBOTs for disaggregating proteins. Moreover, amyloid sizes measured by TEM and DLS are similar in size and shape to the ones with BTO NPs. Consequently, the piezoelectric properties of the BTO NPs are preserved in the PiezoBOTs without affecting the spirulina biotemplate (Fig. S9†), allowing the controlled localization of piezocatalytic NPs to amyloidosis-affected tissues or organs and thereafter disaggregation of amyloid proteins with comparable performance to the BTO NPs.

Last but not least, it is worth mentioning that, compared to other reported piezocatalyst for protein disaggregation,[12] our PiezoBOTs were able to disaggregate the protein with a much shorter ultrasound stimulation exposure (10 minutes *vs.* several hours). Therefore, these microrobots emerge as a promising tool for targeted amyloid protein dissociation.

Conclusions

In this study, we presented the integration of BTO nanoparticles in a multi-functional biotemplated helical microrobot that can be remotely manipulated by magnetic fields and has ultrasound piezocatalytic capabilities for amyloid species disaggregation. The generation of ROS species triggered by the piezoelectric effect dissociates and shortens the amyloid fibrils, resulting in a reduction of the peptide aggregate size by more than 80%. Furthermore, as we demonstrated, the microrobot can be easily magnetically manipulated to enable the

 This journal is © The Royal Society of Chemistry 2023

Open Access Article. Published on 18 avgust 2023. Downloaded on 8. 01. 2026 04:58:24.
This article is licensed under a Creative Commons Attribution-NonCommercial 3.0 Unported Licence.

actuation of the piezoelectric NPs to specific amyloidosis-affected tissues or organs forgoing any cellular damage. Thus, as a result of their piezocatalytic efficiency and good maneuverability, these biocompatible PiezoBOTs are an excellent platform for conducting minimally invasive amyloidosis therapy.

Author contributions

S. N., R. S.-G., C. F., X. C. and S. P. conceived and designed the experiments. Experiments were performed by S. N., R. S.-G., H. Y., A. V., L. H., C. F., Q. T., S. S., and J. L.-W. The manuscript was written by S. N., R. S.-G., C. F., Q. T., S. S., and S. P. with input from all authors.

Conflicts of interest

S. N. is the co-founder of Inia Biosciences. All other authors have no competing financial interests to declare.

Acknowledgements

We acknowledge the Fulbright Program and the Swiss Federal Commission for Scholarships for Foreign Students for supporting this work. The authors would like to thank the Scientific Center for Optical and Electron Microscopy (ScopeM) at ETH for their technical support. R. S.-G. thanks the Spanish Ministry of Universities and the European Union for the 'Margarita Salas' postdoctoral fellowship. Partial funding from a Consolidator Grant from the European Research Council (ERC) under the European Union's Horizon 2020 Research and Innovation Programme (Grant Agreement no. 771565) and Swiss National Science Foundation (SNSF) (no. 192012) is acknowledged. Partial support from SNSF-Sinergia project (no. 198643) is also acknowledged.

Notes and references

1 G. Merlini and V. Bellotti, *N. Engl. J. Med.*, 2003, **349**, 583.
2 M. D. Benson and T. Uemichi, *Amyloid*, 1996, **3**, 44.
3 V. Bellotti, P. Mangione and G. Merlini, *J. Struct. Biol.*, 2000, **130**, 280.
4 J. Floege and M. Ketteler, *Kidney Int.*, 2001, **59**, S164.
5 R. A. Kyle, M. A. Gertz, P. R. Greipp, T. E. Witzig, J. A. Lust, M. Q. Lacy and T. M. Therneau, *N. Engl. J. Med.*, 1997, **336**, 1202.
6 A. D. Wechalekar, J. D. Gillmore and P. N. Hawkins, *Lancet*, 2016, **387**, 2641.
7 T. Popkova, R. Hajek and T. Jelinek, *Br. J. Haematol.*, 2020, **189**, 228.
8 M. Ueda and Y. Ando, *Transl. Neurodegener.*, 2014, **3**, 19.
9 Q. Tang, J. Wu, D. Kim, C. Franco, A. Terzopoulou, A. Veciana, J. Puigmartí-Luis, X. Chen, B. J. Nelson and S. Pané, *Adv. Funct. Mater.*, 2022, **32**, 2202180.
10 S. Han, D. Chen, J. Wang, Z. Liu, F. Liu, Y. Chen, Y. Ji, J. Pang, H. Liu and J. Wang, *Nano Energy*, 2020, **72**, 104688.
11 Y. Zhang, Y. Liu and Z. L. Wang, *Adv. Mater.*, 2011, **23**, 3004.
12 A. Cafarelli, A. Marino, L. Vannozzi, J. Puigmartí-Luis, S. Pané, G. Ciofani and L. Ricotti, *ACS Nano*, 2021, **15**, 11066.
13 L. Liang, C. Sun, R. Zhang, S. Han, J. Wang, N. Ren and H. Liu, *Nano Energy*, 2021, **90**, 106634.
14 M. Hoop, X.-Z. Chen, A. Ferrari, F. Mushtaq, G. Ghazaryan, T. Tervoort, D. Poulikakos, B. Nelson and S. Pané, *Sci. Rep.*, 2017, **7**, 4028.
15 M. Dong, X. Wang, X. Chen, F. Mushtaq, S. Deng, C. Zhu, H. Torlakcik, A. Terzopoulou, X. Qin, X. Xiao, J. Puigmartí-Luis, H. Choi, A. P. Pêgo, Q. Shen, B. J. Nelson and S. Pané, *Adv. Funct. Mater.*, 2020, **30**, 1910323.
16 K. Kapat, Q. T. H. Shubhra, M. Zhou and S. Leeuwenburgh, *Adv. Funct. Mater.*, 2020, **30**, 1909045.
17 F. Mushtaq, H. Torlakcik, Q. Vallmajo-Martin, E. C. Siringil, J. Zhang, C. Röhrig, Y. Shen, Y. Yu, X.-Z. Chen, R. Müller, B. J. Nelson and S. Pané, *Appl. Mater. Today*, 2019, **16**, 290.
18 P. Zhu, Y. Chen and J. Shi, *Adv. Mater.*, 2020, **32**, 2001976.
19 M. Ahamed, M. J. Akhtar, M. A. M. Khan, H. A. Alhadlaq and A. Alshamsan, *Nanomaterials*, 2020, **10**, 2309.
20 J. Jang and C. B. Park, *Sci. Adv.*, 2022, **8**, eabn1675.
21 J. Jang, K. Kim, J. Yoon and C. B. Park, *Biomaterials*, 2020, **255**, 120165.
22 V. Sanna and M. Sechi, *ACS Med. Chem. Lett.*, 2020, **11**, 1069.
23 E. M. Hotze, T. Phenrat and G. V. Lowry, *J. Environ. Qual.*, 2010, **39**, 1909.
24 L. Arms, D. W. Smith, J. Flynn, W. Palmer, A. Martin, A. Woldu and S. Hua, *Front. Pharmacol.*, 2018, **9**, 802.
25 S. Guo, Q. Pan and M. B. Khamesee, *Microsyst. Technol.*, 2008, **14**, 307.
26 A. Chałupniak, E. Morales-Narváez and A. Merkoçi, *Adv. Drug Delivery Rev.*, 2015, **95**, 104.
27 T. M. Alfareed, Y. Slimani, M. A. Almessiere, M. Nawaz, F. A. Khan, A. Baykal and E. A. Al-Suhaimi, *Sci. Rep.*, 2022, **12**, 14127.
28 B. Ertuğ, *Am. J. Eng. Res.*, 2013, **2**, 1–7.
29 X. Wang, X. Deng, H. Wen and L. Li, *Appl. Phys. Lett.*, 2006, **89**, 162902.
30 A. Terzopoulou, M. Palacios-Corella, C. Franco, S. Sevim, T. Dysli, F. Mushtaq, M. Romero-Angel, C. Martí-Gastaldo, D. Gong, J. Cai, X. Chen, M. Pumera, A. J. deMello, B. J. Nelson, S. Pané and J. Puigmartí-Luis, *Adv. Funct. Mater.*, 2022, **32**, 2107421.
31 X.-Z. Chen, J.-H. Liu, M. Dong, L. Müller, G. Chatzipirpiridis, C. Hu, A. Terzopoulou, H. Torlakcik, X. Wang, F. Mushtaq, J. Puigmartí-Luis, Q.-D. Shen, B. J. Nelson and S. Pané, *Mater. Horiz.*, 2019, **6**, 1512.
32 X. Wang, X. Chen, C. C. J. Alcântara, S. Sevim, M. Hoop, A. Terzopoulou, C. de Marco, C. Hu, A. J. de Mello, P. Falcaro, S. Furukawa, B. J. Nelson, J. Puigmartí-Luis and S. Pané, *Adv. Mater.*, 2019, **31**, 1901592.

Open Access Article. Published on 18 avgust 2023. Downloaded on 8. 01. 2026 04:58:24.
This article is licensed under a Creative Commons Attribution-NonCommercial 3.0 Unported Licence.

33 D. Gong, L. Sun, X. Li, W. Zhang, D. Zhang and J. Cai, *Small Struct.*, 2023, 2200356.
34 M. Levy, N. Luciani, D. Alloyeau, D. Elgrabli, V. Deveaux, C. Pechoux, S. Chat, G. Wang, N. Vats, F. Gendron, C. Factor, S. Lotersztajn, A. Luciani, C. Wilhelm and F. Gazeau, *Biomaterials*, 2011, **32**, 3988.
35 L. Lartigue, D. Alloyeau, J. Kolosnjaj-Tabi, Y. Javed, P. Guardia, A. Riedinger, C. Péchoux, T. Pellegrino, C. Wilhelm and F. Gazeau, *ACS Nano*, 2013, **7**, 3939.
36 X. Wang, C. Hu, S. Pan and B. J. Nelson, *IEEE Robot. Autom. Lett.*, 2020, **7**, 1682.
37 Z. Yu, Q. Li, J. Wang, Y. Yu, Y. Wang, Q. Zhou and P. Li, *Nanoscale Res. Lett.*, 2020, **15**, 115.
38 J. B. Schulz, J. Lindenau, J. Seyfried and J. Dichgans, *Eur. J. Biochem.*, 2000, **267**, 4904.
39 L. Micheli, G. Collodel, E. Moretti, D. Noto, A. Menchiari, D. Cerretani, S. Crispino and C. Signorini, *Redox Rep.*, 2021, **26**, 18.
40 B. Hildebrandt, P. Wust, O. Ahlers, A. Dieing, G. Sreenivasa, T. Kerner, R. Felix and H. Riess, *Crit. Rev. Oncol. Hematol.*, 2002, **43**, 33.
41 J. Razzokov, M. Yusupov and A. Bogaerts, *Sci. Rep.*, 2019, **9**, 5476.
42 S. Kang, T. Huynh, Z. Xia, Y. Zhang, H. Fang, G. Wei and R. Zhou, *J. Am. Chem. Soc.*, 2013, **135**, 3150.
43 M. E. Compeán-Jasso, F. Ruiz, J. R. Martínez and A. Herrera-Gómez, *Mater. Lett.*, 2008, **62**, 4248.
44 Q. Tang, J. Wu, D. Kim, C. Franco, A. Terzopoulou, A. Veciana, J. Puigmartí-Luis, X. Chen, B. J. Nelson and S. Pané, *Adv. Funct. Mater.*, 2022, **32**, 2202180.

This journal is © The Royal Society of Chemistry 2023